Supporting information:

First-Principles Elucidation of Defect-Mediated Li Transport in Hexagonal Boron Nitride

Yilong Zhou[1,2,*], S. O. Kucheyev[1], and Liwen F. Wan[1,2,*]

1. Materials Science Division, Lawrence Livermore National Laboratory, Livermore, California 94550, United States
2. Laboratory for Energy Applications for the Future (LEAF), Lawrence Livermore National Laboratory, Livermore, California 94550, United States

* E-mails: zhou17@llnl.gov, wan6@llnl.gov

Methods

Computational details. To investigate the structural and transport properties of Li-BN systems, non-spin polarized density functional theory (DFT) calculations were performed with the projector-augmented wave (PAW) method within the Vienna Ab initio Simulation Package (VASP).[1] The Generalized Gradient Approximation (GGA) with the Perdew−Burke−Ernzerhof (PBE) parametrization was employed for the exchange-correlation functional.[2] The energy cutoff of the plane-wave basis was set to 500 eV. To simulate point defects and Li intercalation, we employed a 6×6×3 supercell of hBN (Fig. 1a), adopting the AA' stacking sequence, which is the thermodynamically most stable configuration for hBN. The first Brillouin zone was approximated with a Γ-only k-point sampling. The energy convergence criterion during electronic relaxation was set to 10^{-5} eV. For geometry relaxation, a tolerance of 0.01 eV/Å was imposed in the atomic forces. Additionally, the dispersion correction accounting for van der Waals interactions was included through Grimme's DFT-D3 method (Table S5).[3] The lattice constants of relaxed hBN were found to be in good agreement with previous experimental and theoretical studies.[4-8] The unit cell of pristine hBN was optimized to a hexagonal lattice of a = 2.509 Å and c = 6.712 Å, with a c/a ratio of 2.675. The equilibrium bond length of B-N is obtained as 1.449 Å, which is consistent with previous experimental and theoretical studies.[4-8]

Four types of vacancy defects (B, N, BN, and B_3N vacancies) were examined in this study. The vacancies were created by removing a single B atom, a N atom, a B-N atom pair, or a B_3N atom cluster from fully optimized pristine hBN. The geometry of the defective hBN was then relaxed. Resultant relaxed structures in the defective BN layer are shown in Fig. 1b.

To investigate the diffusion of Li in both pristine and defective hBN, we employ the climbing image nudged elastic band (cNEB) method,[9,10] implemented in VASP,[1] for finding saddle points and minimum energy paths. For these NEB calculations, the lattice and atomic positions of the start and end point configurations were fully relaxed, while for the intermediate images, only the atomic positions were relaxed. The number of images used in this study was carefully chosen to ensure numerical convergency and efficiency.

Calculations of formation energy. The stability of vacancy defects can be evaluated by computing their formation energies as follows

$$E_{\mathrm{f,d}} = E_{\mathrm{BN}}^{\mathrm{d}} - E_{\mathrm{BN}}^{\mathrm{p}} + n_{\mathrm{B}}\mu_{\mathrm{B}} + n_{\mathrm{N}}\mu_{\mathrm{N}}, \quad (1)$$

where $E_{\mathrm{BN}}^{\mathrm{d}}$ and $E_{\mathrm{BN}}^{\mathrm{p}}$ are total energies of defective hBN with vacancies and pristine hBN, respectively; n_{B} and n_{N} are the number of the removed B and N atoms; and μ_{B} and μ_{N} are the chemical potential of B and N, respectively. Here, we follow the approach used in prior studies

and calculate the formation energy under N-rich conditions.[7,11] As a result, μ_{N} is referenced to the total energy of a N atom in a N_2 molecule, and μ_{BN} is the total energy of a BN atom pair in a BN monolayer (see Fig. S11). μ_{B} is then obtained by subtracting μ_{N} from μ_{BN} as $\mu_{\mathrm{B}} = \mu_{\mathrm{BN}} - \mu_{\mathrm{N}}$.

To assess the stability of Li intercalation in pristine or defective hBN, we calculated the formation energy of Li intercalation as follows

$$E_{\mathrm{Li-int},i} = E^{i}_{\mathrm{Li-BN}} - E^{i}_{\mathrm{BN}} - n_{\mathrm{Li}}E_{\mathrm{Li}}, \quad (2)$$

where i represents "p" or "d" indicating pristine or defective hBN. $E^{i}_{\mathrm{Li-BN}}$ is the total energy of Li-intercalated hBN. n_{Li} is the number of Li atoms, and E_{Li} is the single-atom energy of bulk Li with bcc structure.

Charge density difference analysis. To delve into the electronic intricacies of Li bonding with hBN, we examine charge redistribution resulting from the Li intercalation in hBN using the charge density differences defined as

$$\Delta\rho = \rho_{\mathrm{Li-BN}} - [\rho_{\mathrm{BN}} + \rho_{\mathrm{Li}}], \quad (3)$$

where $\rho_{\mathrm{Li-BN}}$, ρ_{BN}, and ρ_{Li} represent the real-space electronic charge distribution of the total system (Li-intercalated hBN), the Li-free hBN, and the isolated Li located at the same position as in the total system, respectively.

Bader charge analysis. The Bader charge analyses were conducted with the code developed by Henkelman's group, which offers an efficient approach to partitioning a charge density grid obtained from DFT calculations into Bader volumes.[12-14] The charges encapsulated within these Bader volumes provide a reliable approximation of the total electronic charge of an atom.

In-Plane Diffusion of Two Li

We extended our investigation to in-plane diffusion of two Li atoms (Fig. S8), where one Li diffuses alongside another nearby Li. Fig. S8a presents this diffusion in pristine hBN, with one Li intercalating at an H site, while the other Li migrating along an H-E-H path. Compared to the case of a single diffusing Li atom (Fig. 2b), the presence of a nearby Li significantly reduces the forward diffusion energy barrier to 0.1 eV, and even the backward diffusion energy barrier is lower than that in the single Li case.

Fig. S8b shows two-Li diffusion in the presence of a single B vacancy. With one Li trapped at the V site, the other Li migrating along an H-T-H path reveals a greatly reduced activation energy required for Li to escape the vacancy region (see path 2 in Fig. 4a).

Fig. S8c illustrates diffusion in the presence of a single N vacancy, with both Li atoms intercalating at H sites surrounding the N vacancy. Interestingly, when one Li diffuses from its H site to another equivalent H site, the other Li experiences a strong correlated motion and rotates around the N vacancy site with Li-V_N-Li arranged in a line (insets in Fig. S8c). This correlation possibly arises from the tendency for the two Li to stay as far apart as possible to minimize unfavorable electrostatic repulsions, leading to a higher energy barrier of 0.45 eV compared to 0.28 eV in the single Li case (Fig. 4c).

Fig. S8d illustrates the diffusion in the presence of a BN vacancy cluster. Once a Li is trapped at the V site, the BN vacancy no longer serves as a stable intercalation site for another Li. Therefore, we explored the diffusion of Li originating from an H site further away. No significant difference was observed in the diffusion between the two-Li and single Li cases (see the second peak in path 2 in Fig. S9a), possibly because the path is distant from the trapped Li in the vacancy.

Table S1. Formation energy $E_{\mathrm{Li-int,p}}$ of Li intercalation in pristine hBN at the hollow (H), top (T) and edge (E) sites.

	H	T	E
$\boldsymbol{E_{\mathrm{Li-int,p}}}$ (eV)	1.763	2.152	2.099

Table S2. Formation energy $E_{\mathrm{f,d}}$ of defective hBN with single B vacancy ($\mathrm{V_B}$), single N vacancy ($\mathrm{V_N}$), BN pair vacancy ($\mathrm{V_{BN}}$) and B_3N cluster vacancy ($\mathrm{V_{B_3N}}$).

Defective hBN	$\boldsymbol{E_{\mathrm{f,d}}}$ (eV)
$\mathbf{V_B}$	7.830
$\mathbf{V_N}$	7.861
$\mathbf{V_{BN}}$	9.008
$\mathbf{V_{B_3N}}$	14.079

Table S3. Formation energy $E_{\mathrm{Li-int,d}}$ of Li intercalation in defective hBN with $\mathrm{V_B}$, $\mathrm{V_N}$, $\mathrm{V_{BN}}$ and $\mathrm{V_{B_3N}}$ at their corresponding favorite sites shown in Figure 3a.

Defective hBN	$\boldsymbol{E_{\mathrm{Li-int,d}}}$ (eV)
$\mathbf{V_B}$	-3.068
$\mathbf{V_N}$	0.227
$\mathbf{V_{BN}}$	-2.311
$\mathbf{V_{B_3N}}$	-2.298

Table S4. Formation energy $E_{\mathrm{Li-int,d}}$ of Li intercalation in a layer away from a B vacancy at a T site (T0) directly above the B vacancy (a), a T site (T1) adjacent to T0 (b), and a neighboring H site (H0).

	T0	T1	H0
$\boldsymbol{E_{\mathrm{Li-int,d}}}$ (eV)	-0.733	-1.743	-1.148

Table S5. Lattice parameters (Å) of hBN with respect to various vdW corrections.

vdW corrections	$\boldsymbol{a = b}$	$\boldsymbol{c}$	$\boldsymbol{c/a}$
DFT-D2	2.509	6.162	2.456
DFT-D3	2.509	6.712	2.675
Tkatchenko-Scheffler method with iterative Hirshfeld partitioning	2.508	6.742	2.688
Many-body dispersion energy	2.504	6.647	2.655
optB86b-vdW	2.512	6.463	2.573

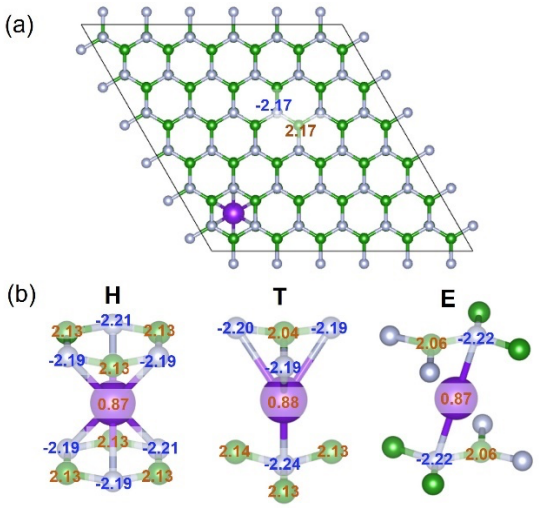

Figure S1. Bader charge analysis of Li intercalation in pristine hBN. (a) Top view of Li interaction in a H site. The charge of a pair of BN away from the Li is marked. (b) Li intercalating the three high-symmetry sites, with charges of corresponding atoms indicated. Bader charge analysis reveals a polarized B-N bond in hBN, with N tending to be negatively charged and B positively charged. With Li maintaining a positive charge across all intercalation sites, the intercalation of Li induces a shift in the charge distribution of neighboring atoms, causing increased negative charges of surrounding N and reduced positive charges of B. In the H site, Li can maintain the greatest distance from surrounding B, thereby mitigating the adverse repulsion between positively charged Li and B. In contrast, in the T site, Li is constrained to stay in closer proximity with B directly connecting to it, and in the E site, Li assumes an intermediate distance from surrounding B. Accordingly, the layer spacing near Li (see Fig. 2a) is maximally enlarged in the T site (3.95 Å), followed by the E site (3.85 Å), and then the H site (3.50 Å), compared to the layer spacing without Li intercalation at 3.36 Å.

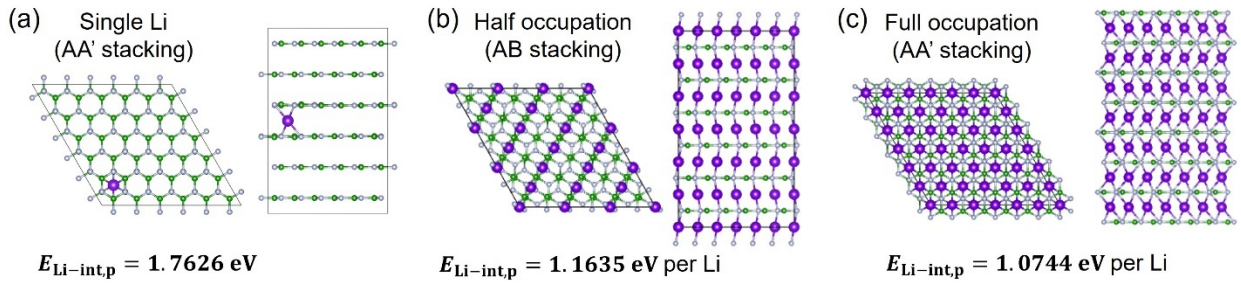

Figure S2. Top (left) and side (right) views of the optimized structures of Li intercalations in pristine hBN. (a-c) Li intercalating a single H site (a), half of the H sites (b), and all H sites (c) within hBN. The stacking sequences of hBN layers undergo transitions from AA' to AB to AA' as the concentrations increase. The formation energy ($E_{\mathrm{Li-int,\,p}}$) of such intercalations decreases with the increase in the Li concentrations.

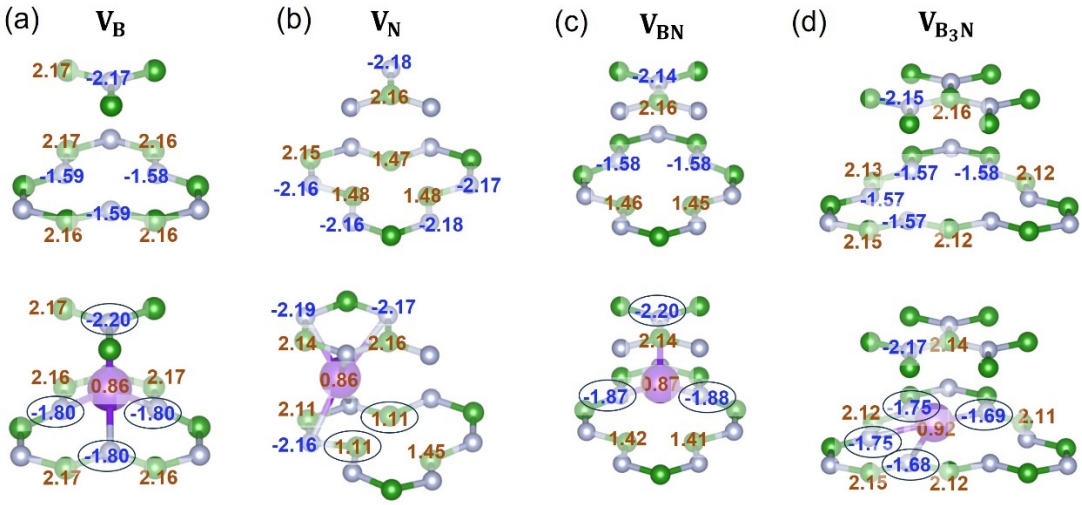

Figure S3. Bader charge analysis of defective hBN with (bottom) and without (top) Li intercalation. (a) B vacancy. (b) N vacancy. (c) BN vacancy. (d) B_3N vacancy. Charges of corresponding atoms are labeled. Black circles highlight the atoms that undergo significant changes in their charges induced by Li intercalation.

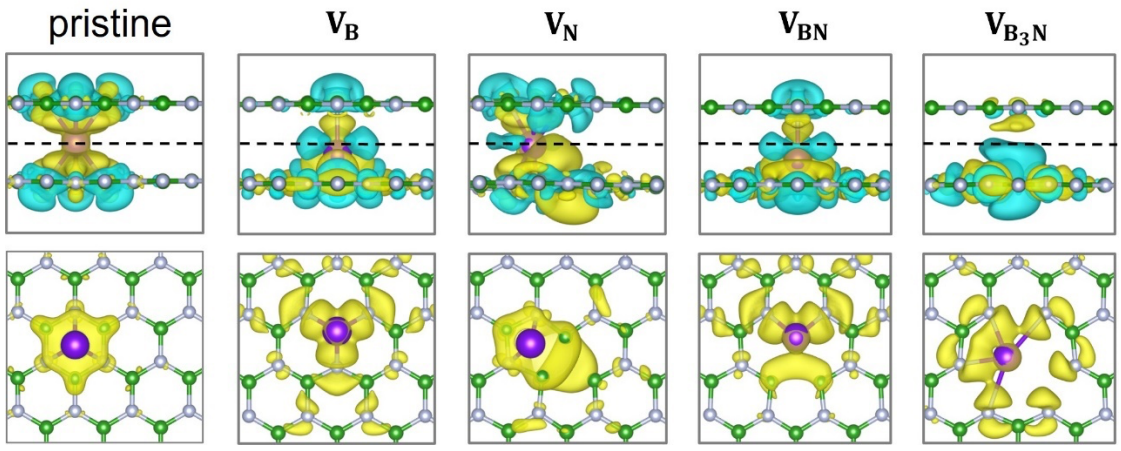

Figure S4. Side (top) and top (bottom) views of charge density difference for Li intercalations at the preferred sites in pristine and defected hBN. Isosurfaces are obtained at 7 × 10−3 e/Å³. Yellow and blue indicate positive and negative charge density differences, respectively. The top view displays only the bottom half of the side view (divided by the black dashed line), with negative charge density differences omitted for clarity. In pristine hBN, the analysis of charge density difference (Eq. 3) in the H site reveals electron accumulation sandwiched between Li and BN layers, which effectively shrinks the size of the hexagonal hole, thereby blocking Li penetration through BN layers. N vacancy (V_N) shows similar electron accumulation between Li and the BN layer, but it spreads out toward the vacancy. This spreading lowers the magnitude of the barrier compared to pristine hBN. The analysis of charge density difference in the presence of V_B,V_{BN}, and V_{B_3N} shows that electron accumulation spreads over a larger region and the empty space surrounding Li increases in response to the larger vacancy size.

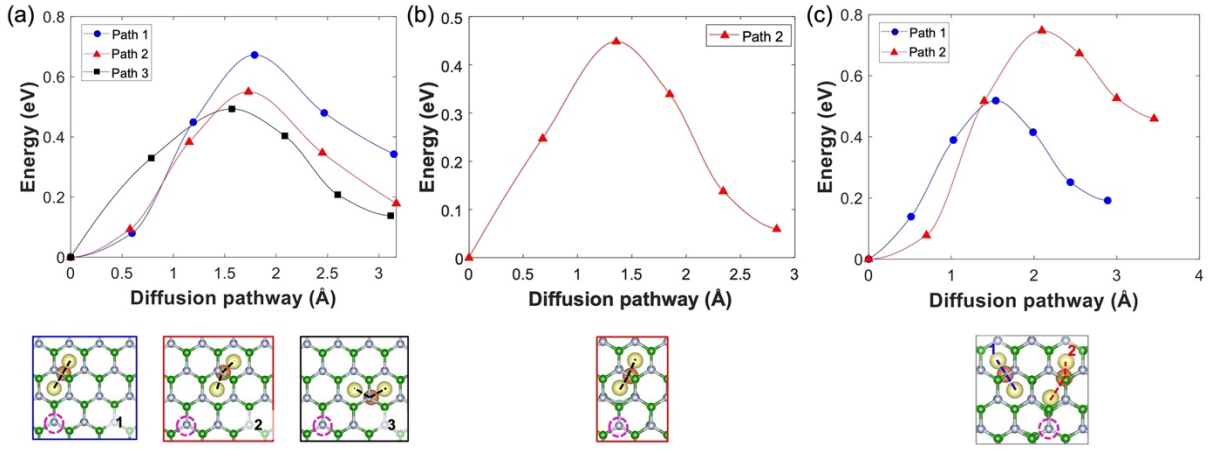

Figure S5. Energy profiles for Li migration in hBN in the presence of B or N vacancies, focusing on the second segments depicted in Figures 4a, 4b, and 4d. (a) Second segments of the energy profiles from Figure 4a along three distinct pathways. (b) Second segment of the energy profile for path 2 in Figure 4b. (c) Second segment of the energy profile in Figure 4d. Associated activation energies (E_a) are labeled. Insets show the corresponding minimum energy diffusion pathways (yellow spheres indicate the initial, local-minimum, and final states; brown spheres indicate the saddle points), with the positions of vacancy highlighted by pink dashed circles.

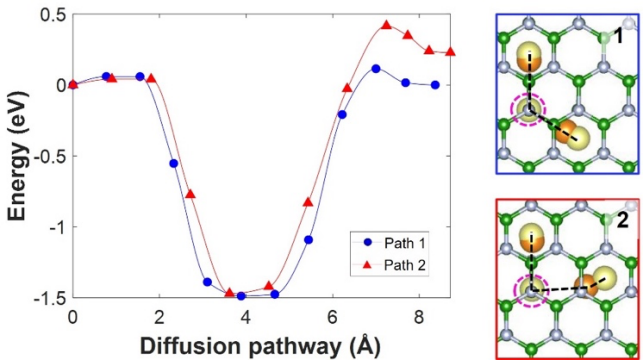

Figure S6. Energy profiles of Li in-plane migrations around B vacancy. Two initial pathways that are linearly interpolated between the starting and ending configurations: one near the B vacancy (path 1) and the other further away (path 2) was investigated. The NEB calculations revealed that the final optimized paths significantly deviated from the initial paths and consistently passed through the B vacancy site. The fact that the significant deviation of the final paths from the initial ones, combined with the presence of the vacancy along the paths, introduced additional challenges for the NEB calculations, leading to slight deviations and asymmetry (path 1) in the energy plots. Insets show the corresponding minimum energy diffusion pathways (yellow spheres indicate the initial, local-minimum, and final states; brown spheres indicate the saddle points), with the positions of vacancy highlighted by pink dashed circles.

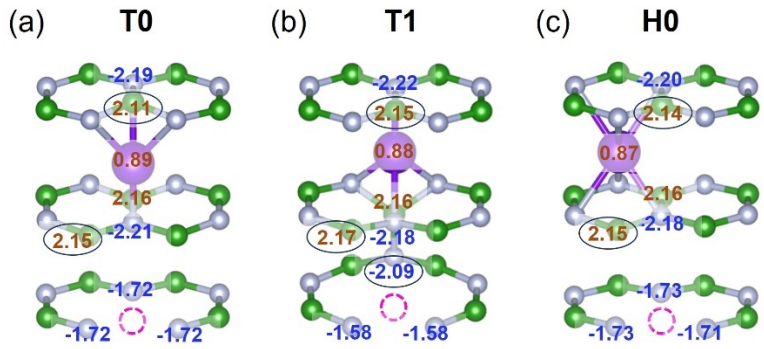

Figure S7. Bader charge analysis of Li intercalation in a layer away from the vacancy. (a-c) Li intercalating a T site (T0) directly above the B vacancy (a), a T site (T1) adjacent to T0 (b), and a neighboring H site (c). Charges of corresponding atoms are labeled, with the charges of representative atoms highlighted by black circles. Pink dashed circles indicate the position of the B vacancy. The charges of B atoms surrounding the Li atom at the T1 site remain largely unaffected, while the N atom forming the BN bridge gains electrons. These findings establish T1 as a more favorable intercalation site for the Li, as supported by the calculated formation energy (Table S4).

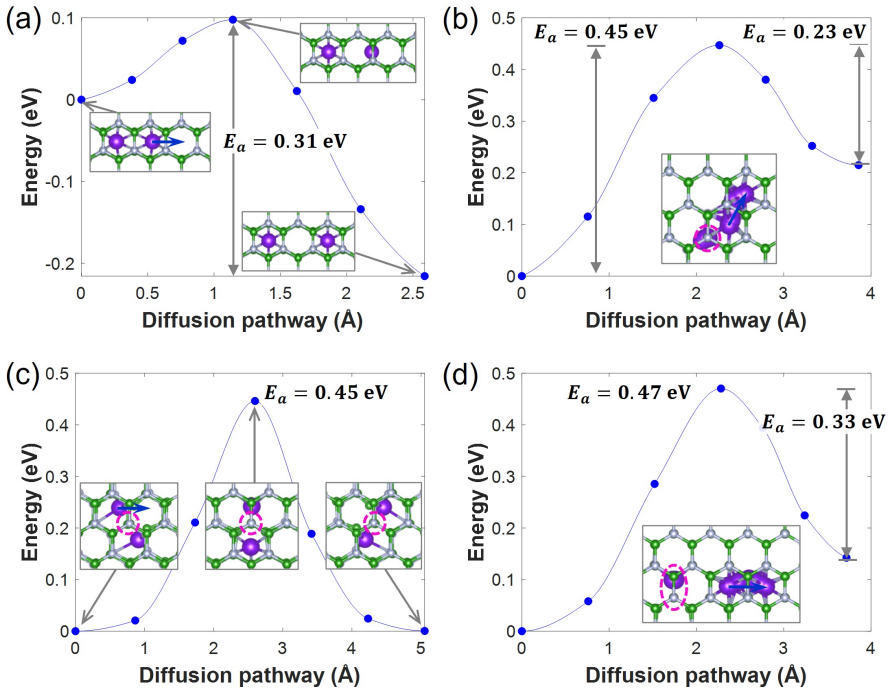

Figure S8. Representative cases of Li diffusion alongside another nearby Li. (a-d) Energy profiles of Li migrations in pristine hBN (a) and defective hBN with B vacancy (b), N vacancy (c), and BN vacancy (d), with associated activation energies (E_a) labeled. Insets in (a) and (c) present atomic configurations associated with corresponding images. Insets in (b) and (d) indicate the migration diffusion pathways. Pink dashed circles highlight the vacancy positions.

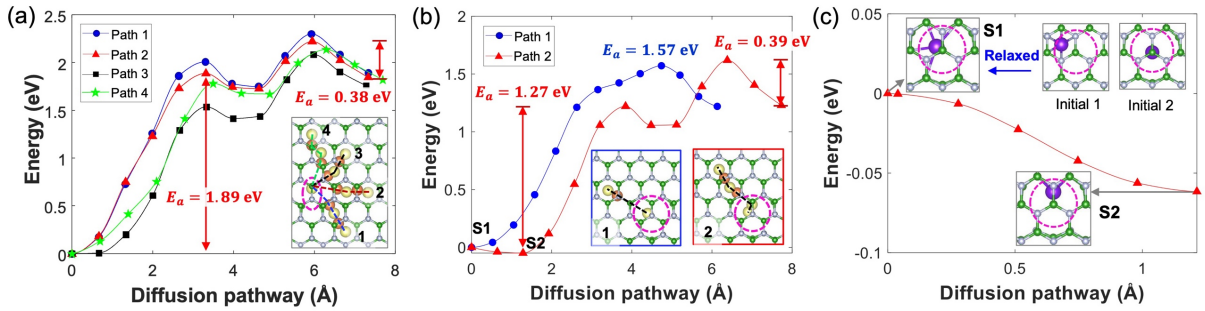

Figure S9. Li in-plane diffusion in the presence of BN and B_3N vacancies. (a, b) Energy profiles of Li migrations in the presence of BN (a) and B_3N (b) vacancies, with associated activation energies (E_a) labeled. Insets show the corresponding minimum energy diffusion pathways (yellow spheres indicate the initial, local-minimum, and final states; brown spheres indicate the saddle points), with the positions of vacancies highlighted by pink dashed circles. A careful examination of the initial stage (within the range of 0 to 1.3 Å) of path 2 in (b)—where Li migrates from between two B vacant sites (S1; inset in (c)) to a B vacant site (S2; inset in (c))—reveals a decline in energy, suggesting that the B vacant site (S2) is an even more stable intercalation site. (c) Energy profile of Li in-plane diffusion from the S1 site to the S2 site obtained through a refined NEB calculation. Insets on the top show relaxation of Li starting from two initial positions: an H site and a T site, both converging to the S1 site. Hence, the B_3N vacancy offers two types of stable intercalation sites.

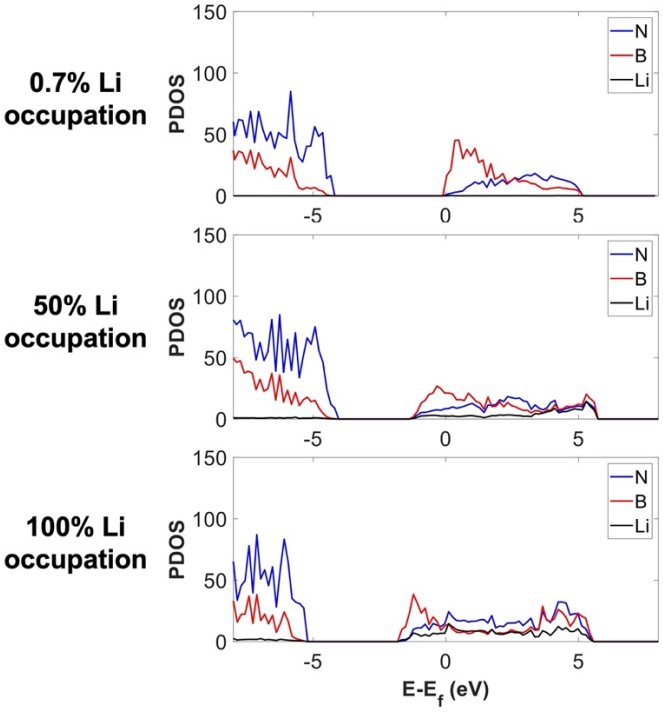

Figure S10. Partial density of states (PDOS) of pristine hBN with Li intercalation at three different concentrations: 0.7%, 50%%, and 100% occupations of the H sites within the lattice. As increasing Li concentration, hBN lattice becomes electronically conductive although the bonding characteristic of B-N is maintained.

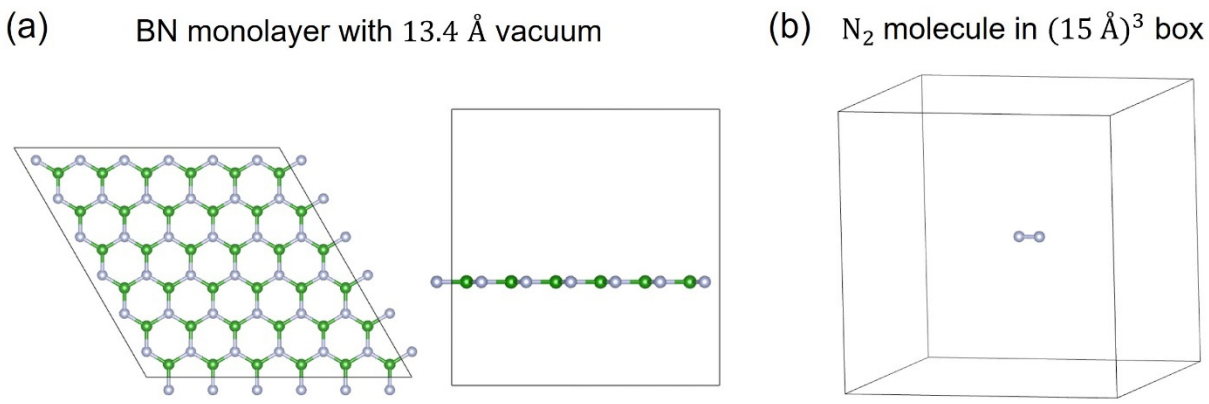

Figure S11. Simulated systems for calculating chemical potentials of B (μ_B) and N (μ_N) atoms. (a) Top (left) and side (right) views of a hBN monolayer. (b) A N_2 molecule in the simulation box. μ_N is then calculated as the total energy of the N_2 molecule divided by 2. The chemical potential of the BN pair (μ_{BN}) is determined by the total energy of the BN monolayer divided by the number of BN pairs. μ_B is subsequently obtained by subtracting μ_N from μ_{BN} as $\mu_B = \mu_{BN} - \mu_N$.

References

1 Kresse, G. & Furthmüller, J. Efficient iterative schemes for ab initio total-energy calculations using a plane-wave basis set. *Physical review B* **54**, 11169 (1996).

2 Perdew, J. P., Burke, K. & Ernzerhof, M. Generalized gradient approximation made simple. *Physical review letters* **77**, 3865 (1996).

3 Grimme, S., Antony, J., Ehrlich, S. & Krieg, H. A consistent and accurate ab initio parametrization of density functional dispersion correction (DFT-D) for the 94 elements H-Pu. *The Journal of chemical physics* **132**, 15 (2010).

4 Paszkowicz, W., Pelka, J., Knapp, M., Szyszko, T. & Podsiadlo, S. Lattice parameters and anisotropic thermal expansion of hexagonal boron nitride in the 10–297.5 K temperature range. *Applied Physics A* **75**, 431-435 (2002).

5 Ooi, N., Rajan, V., Gottlieb, J., Catherine, Y. & Adams, J. B. Structural properties of hexagonal boron nitride. *Modelling and Simulation in Materials Science and Engineering* **14**, 515-535, doi:10.1088/0965-0393/14/3/012 (2006).

6 Weston, L., Wickramaratne, D., Mackoit, M., Alkauskas, A. & Van de Walle, C. G. Native point defects and impurities in hexagonal boron nitride. *Physical Review B* **97**, 214104, doi:10.1103/PhysRevB.97.214104 (2018).

7 Strand, J., Larcher, L. & Shluger, A. L. Properties of intrinsic point defects and dimers in hexagonal boron nitride. *J Phys Condens Matter* **32**, 055706, doi:10.1088/1361-648X/ab4e5d (2020).

8 Alem, N. *et al.* Atomically thin hexagonal boron nitride probed by ultrahigh-resolution transmission electron microscopy. *Physical review B* **80**, 155425 (2009).

9 Henkelman, G., Uberuaga, B. P. & Jónsson, H. A climbing image nudged elastic band method for finding saddle points and minimum energy paths. *The Journal of chemical physics* **113**, 9901-9904 (2000).

10 Henkelman, G. & Jónsson, H. Improved tangent estimate in the nudged elastic band method for finding minimum energy paths and saddle points. *The Journal of chemical physics* **113**, 9978-9985 (2000).

11 Huang, B. & Lee, H. Defect and impurity properties of hexagonal boron nitride: A first-principles calculation. *Physical Review B* **86**, 245406, doi:10.1103/PhysRevB.86.245406 (2012).

12 Tang, W., Sanville, E. & Henkelman, G. A grid-based Bader analysis algorithm without lattice bias. *Journal of Physics: Condensed Matter* **21**, 084204 (2009).

13 Sanville, E., Kenny, S. D., Smith, R. & Henkelman, G. Improved grid‐based algorithm for Bader charge allocation. *Journal of computational chemistry* **28**, 899-908 (2007).

14 Henkelman, G., Arnaldsson, A. & Jónsson, H. A fast and robust algorithm for Bader decomposition of charge density. *Computational Materials Science* **36**, 354-360 (2006).